Journal of Catalysis 275 (2010) 34–44

Contents lists available at ScienceDirect

Journal of Catalysis

journal homepage: www.elsevier.com/locate/jcat

Promotion by hydrous ruthenium oxide of platinum for methanol electro-oxidation

Jun-Hong Ma [a,b], Yuan-Yuan Feng [b], Jie Yu [b], Dan Zhao [b], An-Jie Wang [a], Bo-Qing Xu [b,*]

[a] State Key Laboratory of Fine Chemicals, Dalian University of Technology, Dalian 116012, China
[b] Innovative Catalysis Program, Key Laboratory of Organic Optoelectronics & Molecular Engineering, Department of Chemistry, Tsinghua University, Beijing 100084, China

ARTICLE INFO

Article history:
Received 19 March 2010
Revised 8 June 2010
Accepted 5 July 2010
Available online 19 August 2010

Keywords:
Methanol electro-oxidation
Electrocatalysis
Platinum catalyst
Hydrous ruthenium oxide
Catalyst promoter

ABSTRACT

Pt–$(RuO_xH_y)_m$ electrocatalysts (m being the atomic Ru/Pt ratio) supported on multi-walled carbon nanotubes, in which amorphous hydrous ruthenium oxide (RuO_xH_y) is the exclusive Ru-containing species, were prepared and comprehensively characterized by X-ray diffraction, X-ray photoelectron spectroscopy, temperature-programmed reduction, thermogravimetric analysis and transmission electron microscopy techniques. Cyclic voltammetry (CV) and chronoamperometry studies of CO stripping and methanol electro-oxidation indicated that the CO tolerance and catalytic activity of Pt improved remarkably by the co-presence of RuO_xH_y. Repeated CV pretreatments in 0.5 M H_2SO_4 up to potentials higher than 0.46 V (vs. SCE) induced significant dissolution of RuO_xH_y, which changed the RuO_xH_y content, Pt–RuO_xH_y proximity and surface structure of Pt, and consequently altered the electrocatalytic activity of Pt in the final electrode. However, RuO_xH_y dissolution was not identified when the pretreatment potentials was set no higher than 0.46 V. Discussion on the promotional function of RuO_xH_y was made based on the peculiarity of RuO_xH_y as a mixed electron/proton conductor.

1. Introduction

Direct methanol fuel cells (DMFCs) are regarded as the most promising new power sources of the future, especially for mobile and portable applications. However, one of the main challenges to make DMFCs commercially feasible is to improve the kinetics of the methanol oxidation reaction at the anode. The advent of the so-called bimetallic PtRu catalysts has led to a big step forward in improving the anode performance of DMFCs [1,2]. Ruthenium in these PtRu catalysts plays, as an effective promoter to Pt, a crucial role in the generation of oxygenated surface species (i.e., Ru–OH) by promoting water dissociation [3]. It is generally understood that these Ru–OH species are essential in lowering potentials for the oxidative removal of CO-like poisoning intermediates from the surfaces of Pt-based anode catalyst [4–6].

In the last decade, many investigations have been conducted to uncover the nature of PtRu anode catalysts. A consensus on the chemical nature or oxidation state of active ruthenium species, however, has not yet reached. While metallic Ru in PtRu alloy entities is often referred to as the active ruthenium species [7,8], ex-situ and in situ physicochemical characterizations have shown that the Ru component at the surface of a PtRu alloy catalyst is partially oxidized due to oxygen uptake from the working environment [9–11]. According to Rolison et al., the as-received commercial PtRu black catalysts (E-TEK and JM), which showed X-ray diffraction (XRD) patterns consistent with an alloy assignment, contained actually a substantial fraction of amorphous hydrous ruthenium oxide (RuO_xH_y or $RuO_2{\cdot}nH_2O$) by thermogravimetry (TG) and X-ray photoelectron spectroscopy (XPS) analyses [12]. In addition, the electrocatalytic activity for methanol electro-oxidation of PtRu blacks rich in RuO_xH_y was found two orders of magnitude higher, in terms of exchange current density, than their reduced (Pt^0Ru^0) and thermally dehydrated (Pt–RuO_2) counterpart catalysts [13]. The superior performance of the RuO_xH_y-rich PtRu catalysts was attributed to the uniqueness of RuO_xH_y as a mixed electron/proton conductor innately related with a Ru–OH speciation [13]. The very beneficial effect of RuO_xH_y in PtRu catalyst on methanol electro-oxidation was thereafter frequently confirmed experimentally in different laboratories [13,14–20]; notwithstanding, it was mentioned occasionally that the formation of RuO_xH_y could be responsible for deterioration of PtRu electrocatalysts [21–23]. In these earlier studies, however, RuO_xH_y in PtRu catalysts was derived either from partial oxidation of the so-called metallic Ru in a PtRu alloy [13,16,17,20] or from electrochemical protonation of a RuO_2 surface [14,18]. In a few cases, the RuO_xH_y was first prepared by oxidation of ruthenium halide, followed by a reductive deposition of Pt to make RuO_xH_y-containing PtRu samples [15,19], during which a partial reduction of the preformed RuO_xH_y to metallic Ru would be inevitable. Thus, it can be understood that RuO_xH_y species in those earlier publications was always "contaminated" with other forms of ruthenium (metallic Ru and/or crystalline RuO_2), which could significantly distort the signature of RuO_xH_y species as a promoter in Pt-based anode catalysts. To better understand the promoter function of RuO_xH_y species, it would

* Corresponding author. Fax: +86 10 62792122.
E-mail address: bqxu@mail.tsinghua.edu.cn (B.-Q. Xu).

0021-9517/$ - see front matter © 2010 Elsevier Inc. All rights reserved.
doi:10.1016/j.jcat.2010.07.021

be essential to check with an anode material that clearly excludes any possible involvement of ruthenium species other than RuO_xH_y.

In this work, a series of multi-walled carbon nanotubes (MWCNTs)-supported Pt–$(RuO_xH_y)_m$ (m being the atomic Ru/Pt ratio, m = 0.04–0.40) anode catalysts are carefully prepared to preclude the presence of any metallic Ru or anhydrous RuO_2. Electrochemical characterizations of these catalysts in relation to methanol electro-oxidation are then conducted to gain insight into the promotional effect of "non-contaminated" RuO_xH_y on Pt catalyst. Our data demonstrate clearly that the "non-contaminated" RuO_xH_y alone can act as a very efficient promoter of Pt for the electro-oxidation of CO and methanol. We also show that the composition (atomic Ru/Pt ratio) and pretreatment potentials are of vital importance to the overall anode performance (activity and stability) of these catalysts.

2. Experimental

2.1. Sample preparation

2.1.1. MWCNTs-supported RuO_xH_y (RuO_xH_y/MWCNTs)

The support MWCNT materials (i.d. 3–5 nm, o.d. 15–45 nm, tube length up to 10 μm), prepared by CH_4 decomposition over a Ni–MgO catalyst [24], were subjected to a pretreatment with concentrated nitric acid to introduce oxygen-containing functional groups [25,26]. RuO_xH_y/MWCNT (Ru loading: 0.5–5.1 wt.%) samples were then prepared by the oxidative precipitation method according to Fu et al. [27]. In a typical procedure, 0.40 g MWCNTs was ultrasonically dispersed for 2 h in 25 mL of 5 mM $RuCl_3$ aqueous solution. Subsequently, 30 mL of aqueous H_2O_2 solution (30%) was added dropwise at room temperature under vigorous stirring. The obtained suspension was further agitated for 8 h at 353 K, followed by separation of the precipitates by filtration and extensive washing with de-ionized water. The obtained solid sample was then dried overnight at 383 K to give RuO_xH_y/MWCNTs. The filtrate was collected and analyzed by inductively coupled plasma mass spectrometry (ICP-MS) to determine the actual loading of RuO_xH_y. A reference RuO_2/MWCNT sample was obtained by calcining the as-prepared RuO_xH_y/MWCNTs (Ru loading: 1.3 wt.%) in flowing dry N_2 at 773 K for 2 h.

2.1.2. Pt–$(RuO_xH_y)_m$/MWCNTs

Pt–$(RuO_xH_y)_m$/MWCNT samples were made by Pt deposition onto RuO_xH_y/MWCNTs with a modified colloidal approach. Briefly, a Pt sulfite complex synthesized from K_2PtCl_6 and $NaHSO_3$ [28] was dissolved in de-ionized water at pH ≈3.0, and RuO_xH_y/MWCNTs and ethanol were then added to form a suspension. Under vigorous stirring and careful maintenance of pH (~3.0) with NaOH solution, H_2O_2 was added dropwise at room temperature to oxidatively decompose the sulfite complex, and the resulting suspension was further refluxed for 2 h to deposit Pt nanoparticles on RuO_xH_y/MWCNTs. After filtration and extensive washing, the solids were finally dried at 383 K to give the Pt–$(RuO_xH_y)_m$/MWCNT catalyst. A similar preparation using MWCNTs instead of RuO_xH_y/MWCNTs produced the reference Pt/MWCNT sample. The Pt loading in Pt–$(RuO_xH_y)_m$/MWCNTs as confirmed by ICP-MS analysis was 20 wt.%. The actual Ru loadings in these samples are 0.4, 1.0, 2.1, 3.1 and 4.1 wt.% with m = 0.04, 0.10, 0.20, 0.30 and 0.40, respectively.

2.2. Physicochemical characterizations

XRD patterns were recorded on a Bruker D8-Advance X-ray diffractometer using a Cu Kα radiation (λ = 0.15406 nm) operating at 40 kV and 40 mA with a scan step of 0.02 deg. XPS spectra were acquired with a PHI 5300 ESCA1610 SAM instrument using Mg Kα radiation. The binding energies (BE) were calibrated using the adventitious C 1s line at 284.6 eV. XPS spectra of Pt 4f and Ru 3p were deconvoluted by using a XPS peak 4.1 software. Gaussian–Lorentzian natural line width and asymmetry parameters were applied for identifying Pt 4f and Ru 3p components. The Shirley background and a least-squares routine were used for peak fit tings. Transmission electron microscopy (TEM) and energy-dispersive X-ray spectroscopy (EDX) measurements were performed on a JEM-2010/EDX instrument operating at 120 kV to determine morphology and size distribution of platinum and ruthenium entities.

Temperature-programmed reduction (TPR) experiment was conducted on a homemade TPR apparatus equipped with a thermal conductivity detector (TCD). Prior to each measurement, 50 mg of the catalyst was pretreated in an Ar flow at 298 K for 30 min, followed by cooling to 163 K (with an ethanol/liquid nitrogen cold trap) in flowing Ar. The pretreated sample was then switched to a flow of 5% H_2/Ar. After waiting for a sufficient long period to obtain a stable baseline (the temperature of the cold trap increased to 193 K during this process), the sample temperature was programmed to ramp at a rate of 10 K min^{-1} up to 700 K. The gases were all carefully dried and de-oxygenated to ensure accurate detection of hydrogen comsumptions. Thermogravimetric analysis (TGA) was carried out on a Mettler-Toledo TG/SDTA 851^e instrument. Samples were loaded into alumina pans and heated from 373 to 1073 K at 10 K min^{-1} in flowing dry N_2 (50 mL min^{-1}).

2.3. Electrochemical measurements

A three-electrode measurement system was employed for electrochemical tests. The working electrode was a piece of carbon paper (Toray, TGPH-120) covered with a thin layer of Nafion-impregnated catalyst. In a standard procedure, the catalyst inks were prepared by mixing 5 mg catalyst sample with 0.25 mL isopropanol, followed by addition of 20 μL 5 wt.% Nafion solution (Aldrich) and ultrasonic dispersion of the mixture for 15 min. The obtained ink was then carefully coated onto a piece of carbon paper (0.5 cm × 2.0 cm) to cover an area of 0.5 cm × 0.5 cm and dried under an infrared lamp. The overall catalyst loading was controlled at 1.0 ± 0.1 mg. Saturated calomel electrode (SCE) and a 1.0 cm × 1.0 cm Pt foil were used as the reference and counter electrodes, respectively. All experiments were done at room temperature in N_2-saturated solutions. The potentials were given with respect to SCE unless otherwise stated. Prior to the electrochemical measurement, the electrode catalyst was pretreated by repeated cyclic voltammetry (CV) scanning in 0.5 M H_2SO_4 for 60 cycles at a scan rate of 50 mV s^{-1}, in either a narrow (−0.20 to 0.46 V) or an extended (−0.20 to 0.96 V) potential range.

CO stripping experiment was carried out in 0.5 M H_2SO_4. The electrolyte solution was initially purged with high-purity dry N_2. Adsorption of CO on the electrode catalyst was conducted by bubbling high purity CO through the electrolyte solution for 15 min, followed by purging with N_2 for 20 min to expel residual CO out of the solution. The CO stripping CV curves were obtained in the potentials between −0.20 and 0.96 V with a scanning rate of 20 mV s^{-1}. CV and chronoamperometry (CA) tests of methanol electro-oxidation reaction were performed in 0.5 M H_2SO_4 + 0.5 M CH_3OH solution. The stable CV curves were recorded with a scanning rate of 20 mV s^{-1}. All the electrochemical tests were carried out with a potentiostat/galvanostat model 263A controlled by PowerSuite software (Princeton Applied Research).

3. Results

3.1. Characterization of ruthenium entities and platinum dispersion

Fig. 1 shows the XRD patterns of Pt/MWCNTs and Pt–$(RuO_xH_y)_m$/MWCNTs (m = 0.10, 0.20 and 0.40). The as-prepared

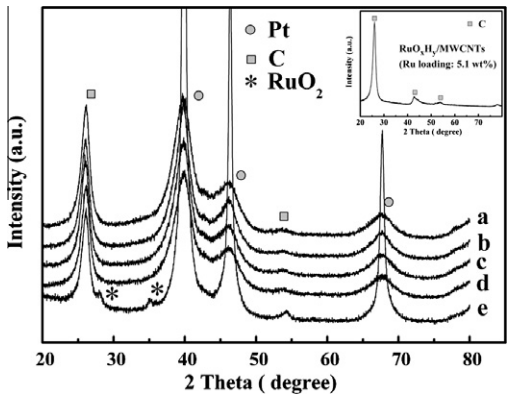

Fig. 1. XRD patterns of (a) Pt/MWCNTs, (b) Pt–$(RuO_xH_y)_{0.10}$/MWCNTs, (c) Pt–$(RuO_xH_y)_{0.20}$/MWCNTs and (d) Pt–$(RuO_xH_y)_{0.40}$/MWCNTs. (e) XRD pattern of Pt–$(RuO_xH_y)_{0.40}$/MWCNTs after thermal treatment in flowing N_2 at 773 K. The inset shows the XRD pattern of a RuO_xH_y/MWCNTs (Ru loading: 5.1 wt.%) without Pt.

Pt–$(RuO_xH_y)_m$/MWCNT samples (Fig. 1b–d) showed diffractions associated with Pt and graphitic carbons; diffractions assignable to the hexagonal close-packed (hcp) structure of metallic Ru or anhydrous tetragonal RuO_2 were not detected. These features were independent of the atomic Ru/Pt ratio (m) of the Pt–$(RuO_xH_y)_m$/MWCNT sample. The diffractions characteristic of the face-centered cubic (fcc) crystallites of Pt in the Pt–$(RuO_xH_y)_m$/MWCNT samples (Fig. 1b–d) were basically unshifted in comparison with those in the Pt/MWCNT (i.e., $m = 0$) sample (Fig. 1a). The average crystallite sizes of Pt, calculated according to Debye–Scherrer equation, were about 2.7 nm in both Pt/MWCNT and Pt–$(RuO_xH_y)_m$/MWCNT samples. These observations suggest that ruthenium species in these as-prepared Pt–$(RuO_xH_y)_m$/MWCNT samples most likely exists as an amorphous phase (i.e., amorphous RuO_xH_y). The inset of Fig. 1 gives the XRD pattern of RuO_xH_y/MWCNTs (Ru loading: 5.1 wt.%), which features diffractions associated only with graphitic carbons and hints that ruthenium species in this zero-platinum RuO_xH_y/MWCNT sample exists also as amorphous RuO_xH_y.

The effect of thermal treatment on the phase composition of Pt–$(RuO_xH_y)_m$/MWCNTs was exemplified by Pt–$(RuO_xH_y)_{0.40}$/MWCNTs before and after the thermal treatment in flowing N_2 at 773 K (Fig. 1d and e). In association with the intensity increase in the Pt peaks, two new diffractions at $2\theta = 28^\circ$ and 35° became evident in the XRD pattern of the thermal-treated sample (Fig. 1e). Consistent with the tetragonal RuO_2 crystals formed from dehydration of amorphous RuO_xH_y [29], these new peaks point to the existence of RuO_xH_y in the as-prepared Pt–RuO_xH_y samples, as would have been expected.

The surface composition and chemical states of Pt and Ru in the as-prepared Pt–$(RuO_xH_y)_m$/MWCNTs were characterized using XPS (Fig. 2). The Pt 4f signals can be deconvoluted into three doublets, among which the most intensive doublet with BE at 71.3 and 74.6 eV was a signature of Pt (0), while the other two doublets (72.5 and 75.8 eV, 74.1 and 77.4 eV) were signatures of Pt (II) and Pt (IV), respectively. A semi-quantitative analysis, based on the integration areas of Pt in varied valence states, showed that around 70% of Pt was in its metallic state for all the investigated Pt–$(RuO_xH_y)_m$/MWCNT samples. The Ru 3p signals of Pt–$(RuO_xH_y)_m$/MWCNTs can be deconvoluted into two peaks at 463.1 and 466.0 eV. These signals remarkably deviated from those of Ru (0) (461.1 eV) and anhydrous RuO_2 (462.4 eV) [30] but match the XPS characteristics of hydrous ruthenium oxide (RuO_xH_y) which was reported to take on a very broad peak showing BE higher than that of its anhydrous form [12]. What really matters to this work is that the XPS spectra for Ru 3p clearly revealed an absence of Ru (0) in any Pt–$(RuO_xH_y)_m$/MWCNT catalysts. The inset of Fig. 2B–c shows the XPS spectrum of Ru 3p for the reference sample RuO_xH_y/MWCNTs (Ru loading: 5.1 wt.%), which confirms that ruthenium species in this reference

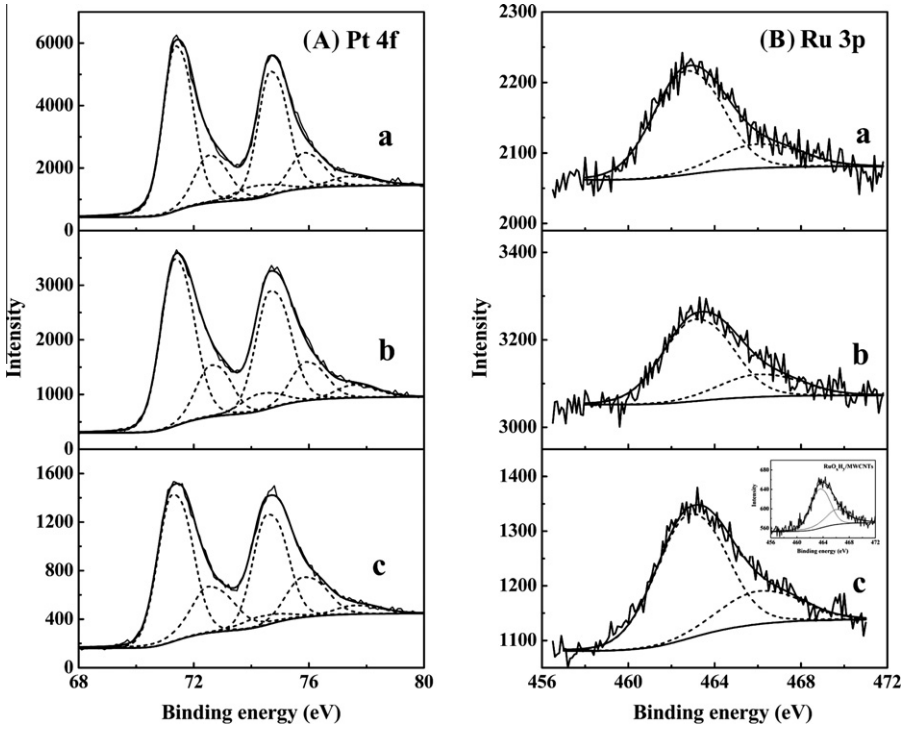

Fig. 2. Pt 4f (A) and Ru 3p (B) XPS spectra of (a) Pt–$(RuO_xH_y)_{0.10}$/MWCNTs, (b) Pt–$(RuO_xH_y)_{0.20}$ /MWCNTs and (c) Pt–$(RuO_xH_y)_{0.40}$/MWCNTs. The inset shows the Ru 3p XPS spectrum of RuO_xH_y/MWCNTs (Ru loading: 5.1 wt.%) without Pt.

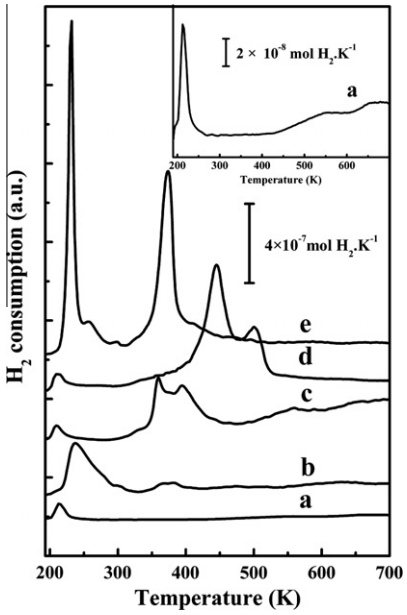

Fig. 3. TPR profiles of (a) MWCNTs, (b) Pt/MWCNTs, (c) RuO_xH_y/MWCNTs (Ru loading: 1.3 wt.%), (d) RuO_2/MWCNTs (Ru loading: 1.3 wt.%) and (e) Pt–$(RuO_xH_y)_{0.10}$/MWCNTs. The inset shows an enlargement of profile (a).

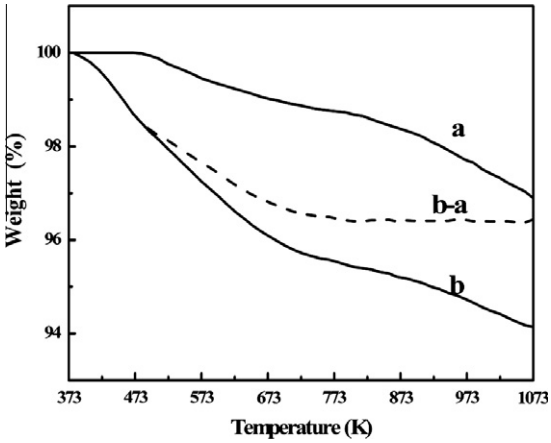

Fig. 4. TG curves of (a) MWCNTs and (b) Pt–$(RuO_xH_y)_{0.40}$/MWCNTs. (b-a) Shows the calibrated weight loss due to the thermal decomposition of oxidic ruthenium species (RuO_xH_y).

sample was also characteristic of RuO_xH_y, same as those in the Pt–$(RuO_xH_y)_m$/MWCNT samples.

Fig. 3 shows the H_2-TPR profiles of MWCNTs, Pt/MWCNTs, RuO_xH_y/MWCNTs (Ru loading: 1.3 wt.%), Pt–$(RuO_xH_y)_{0.10}$/MWCNTs and RuO_2/MWCNTs (Ru loading: 1.3 wt.%). The peak temperature and H_2 consumption data are listed in Table 1. A small but evident peak at about 208 K was observed for every sample in Fig. 3, which was an artifact caused by the ill-controlled temperature increase at the very beginning of the temperature ramp (i.e., in the initial several minutes following removal of the cold trap). The MWCNT support showed no hydrogen consumption up to 430 K, above which hydrogen consumption due to reduction of oxygen-containing surface species such as carboxylic groups on MWCNTs [31] and methanation of carbon became observable (as shown by the inset of Fig. 3). The peak at 237 K on the TPR profile of Pt/MWCNTs was assigned to the reduction of PtO_x; a similar peak was also observed earlier in the TPR of Pt/C oxidized at 300–570 K [32]. The TPR profile of RuO_xH_y/MWCNTs (Fig. 3c) showed two unresolved peaks at 357 and 395 K, different from the TPR profiles of RuO_xH_y in Refs. [19,32] where only one peak at about 370 K was recorded. The unresolved two peaks may arise from inhomogeneous composition of the materials, which would result in varied interactions between RuO_xH_y and MWCNTs. However, the temperature for the reduction of RuO_xH_y in RuO_xH_y/MWCNTs was distinctly lower than that of RuO_2 in the counterpart RuO_2/MWCNT sample (Fig. 3d).

The TPR profile of Pt–$(RuO_xH_y)_{0.10}$/MWCNTs (Fig. 3e) exhibited two peaks centered at 233 and 374 K, which might be attributed to the reduction of PtO_x and amorphous RuO_xH_y, respectively. The temperature for the reduction of RuO_xH_y in this sample agreed with that in the Pt-free RuO_xH_y/MWCNTs (Fig. 3c) but was remarkably lower than the reduction temperature of crystalline RuO_2 in RuO_2/MWCNTs (Fig. 3d). These results might suggest that our Pt–$(RuO_xH_y)_m$/MWCNT samples were made free of crystalline RuO_2.

Calibration of hydrogen consumption for the reduction of ruthenium species in RuO_xH_y/MWCNTs and Pt–$(RuO_xH_y)_m$/MWCNTs disclosed a stoichiometry of H/Ru (molar) ≈ 3.5, which is lower than the reduction stoichiometry (H/Ru = 4.1) of RuO_2 in RuO_2/MWCNTs (Table 1). Therefore, both the peak temperature and hydrogen consumption data of our TPR experiments point to the fact that ruthenium species in our as-prepared samples is in a mixed valence state between +3 and +4, in accordance with a RuO_xH_y (or $RuO_2{\cdot}n$-H_2O) speciation [33,34].

TGA experiment was conducted on Pt–$(RuO_xH_y)_{0.40}$/MWCNTs to measure the content of structural water in RuO_xH_y ($RuO_2{\cdot}nH_2O$) (Fig. 4). To exclude the influence of functional groups on the surface of MWCNTs, a calibrated TG curve (Fig. 4b-a) was obtained by subtracting the weight loss of an equivalent MWCNTs (Fig. 4a) from that of Pt–$(RuO_xH_y)_{0.40}$/MWCNTs (Fig. 4b), and the corrected value was used to determine the weight loss during the thermal dehydration of RuO_xH_y. The result revealed a water content of 3.1 wt.% for RuO_xH_y in Pt–$(RuO_xH_y)_{0.40}$/MWCNTs, which indicates that the hydrous ruthenium oxide can be expressed as a $RuO_2{\cdot}nH_2O$ of $n = 4.1$ or $RuO_{6.1}H_{8.2}$.

Fig. 5 shows the representative TEM images of two RuO_xH_y/MWCNT (Ru loading: 1.3 wt.% and 5.1 wt.%) samples and their Pt-loaded counterparts, Pt–$(RuO_xH_y)_{0.10}$/MWCNTs and Pt–$(RuO_xH_y)_{0.40}$/MWCNTs. A representative TEM image of the ruthenium-free sample Pt/MWCNTs was also included for reference. RuO_xH_y particles in RuO_xH_y/MWCNTs containing 1.3 wt.% Ru were uniformly dispersed on the support MWCNT material, with sizes around 1–2 nm (Fig. 5A). However, the RuO_xH_y particles in the other RuO_xH_y/MWCNTs containing 5.1 wt.% Ru were somewhat aggregated (Fig. 5B). Consequently, the Pt–RuO_xH_y particles in Pt–$(RuO_xH_y)_{0.10}$/MWCNTs appeared also uniformly dispersed, their small sizes (2–3 nm) seen in the TEM images (e.g., Fig. 5C) agreed well with the XRD crystallite size for metallic Pt. In contrast, the

Table 1
H_2 consumption and peak temperatures from TPR experiments.

Sample	Metal loading	Peak temperature (K)	H/Pt (molar ratio)	H/Ru (molar ratio)
Pt/MWCNTs	20.0 wt.% Pt	237	0.6	–
RuO_xH_y/MWCNTs	1.3 wt.% Ru	357, 395	–	3.5
RuO_2/MWCNTs	1.3 wt.% Ru	444, 500	–	4.1
Pt–$(RuO_xH_y)_{0.10}$/MWCNTs	20.0 wt.% Pt, 1.0 wt.% Ru	233, 374	0.6	3.6

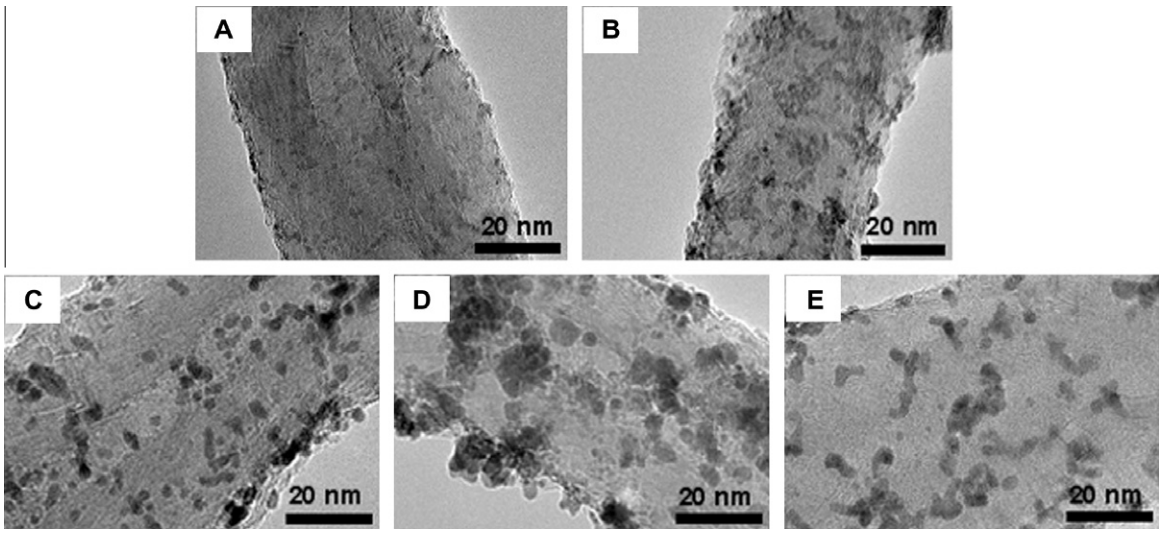

Fig. 5. Representative TEM images of (A) RuO_xH_y/MWCNTs (Ru loading: 1.3 wt.%), (B) RuO_xH_y/MWCNTs (Ru loading: 5.1 wt.%), (C) Pt–$(RuO_xH_y)_{0.10}$/MWCNTs, (D) Pt–$(RuO_xH_y)_{0.40}$/MWCNTs and (E) Pt/MWCNTs. Samples C and D were obtained, respectively, by loading samples A and B with Pt.

Pt–RuO_xH_y particles in Pt–$(RuO_xH_y)_{0.40}$/MWCNTs appeared as ill-dispersed aggregates (Fig. 5D), showing a significantly larger mean particle size (3.8 ± 0.7 nm). These data suggest that the dispersive state of Pt–RuO_xH_y particles in Pt–RuO_xH_y/MWCNTs is closely related with the dispersion of the preloaded RuO_xH_y particles, possibly due to strong interaction of Pt with RuO_xH_y. Moreover, the Pt particles of Pt/MWCNTs (Fig. 5E) were well-dispersed on the carbon support, and their mean particle size (2.8 ± 0.5 nm) was in good agreement with the XRD-derived crystallite size for metallic Pt. The above results indicate that the content of RuO_xH_y has a noticeable effect on the resulting Pt–RuO_xH_y particle size in the Pt–RuO_xH_y catalysts. This is in contrast to the results of Radmilović et al. who showed that the amount of Ru in PtRu alloy catalysts had little effect on the sizes of PtRu particles [35].

The Pt–$(RuO_xH_y)_m$/MWCNT samples were also subjected to EDX analysis in the TEM mode. Although in most of the areas examined the EDX signals of platinum were accompanied with those of ruthenium, areas signifying only Pt were sometimes indeed detected. Such platinum only (or ruthenium silent) areas seemed to decrease with increasing the Ru/Pt ratio (i.e., *m*).

3.2. Electrochemical performance in half-cell measurements

3.2.1. RuO_xH_y/MWCNTs

Fig. 6 shows the CV curves of RuO_xH_y/MWCNTs containing 3.9 wt.% Ru in 0.5 M H_2SO_4 with or without methanol. A pair of broad peaks at 0.40 V (forward scan) and 0.30 V (backward scan), which is indicative of a capacitive behavior associated with the redox and proton conduction properties of RuO_xH_y [36], was observed in the absence of CO and methanol (Fig. 6a). This capacitive behavior remained unchanged in the CO stripping voltammogram (Fig. 6b). The voltammogram recorded in the presence of 0.5 M CH_3OH (Fig. 6c) showed an oxidation current only at potentials above 0.85 V; in the lower potentials, it appeared the same as the blank CV (Fig. 6a). These results demonstrate that RuO_xH_y/MWCNTs itself is not active for the electro-oxidation of either CO or methanol.

The RuO_xH_y/MWCNT (Ru loading: 3.9 wt.%) electrode was pretreated by repeated CV scanning for 60 cycles in 0.5 M H_2SO_4 and 0.5 M H_2SO_4 + 0.5 M CH_3OH, respectively, in either narrow (−0.20 to 0.46 V) or extended (−0.20 to 0.96 V) potential range for understanding the electrochemical stability of RuO_xH_y. Fig. 7 shows the CV curves in 0.5 M H_2SO_4 after such pretreatments. In a fixed pretreatment potential range, the capacitive currents of RuO_xH_y/MWCNT electrodes after the pretreatment in the methanol-containing electrolyte (Fig. 7b and d) were always lower than those obtained after the pretreatment in the methanol-free electrolyte (Fig. 7a and c). The lower capacitive currents after the pretreatments in 0.5 M H_2SO_4 + 0.5 M CH_3OH could be accounted for by a loss of structural water in RuO_xH_y, due to methanol/water exchange [37].

The pretreatment potentials imposed an even larger impact on the capacitive current. Compared with the cases of pretreatment in the narrow potential range (Fig. 7a and b), the capacitive currents decreased severely after the pretreatment in the extended potential range; this was regardless of the absence (Fig. 7c) or presence of methanol in the electrolyte (Fig. 7d). These results provided a qualitative and clear evidence for RuO_xH_y dissolution during the anodic scanning at high potentials (0.46–0.96 V).

Therefore, an estimation of the ruthenium dissolution percentage was made according to the relative capacitance recorded in the potential range of 0.15–0.75 V, the results of which are given in Table 2. ICP-MS analysis of ruthenium dissolved in the electrolyte produced similar numbers, which directly confirmed ruthenium dissolution during the pretreatment in the extended potential range. It is noteworthy, in reference to the CV curve of the

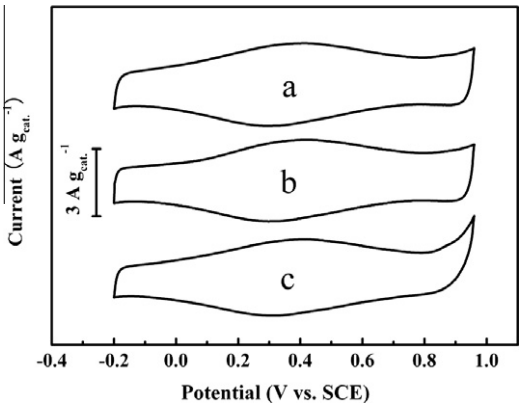

Fig. 6. Cyclic voltammograms of RuO_xH_y/MWCNTs (Ru loading: 3.9 wt.%) in 0.5 M H_2SO_4, (a) blank, (b) after CO adsorption (CO stripping curve) and (c) in the presence of 0.5 M CH_3OH.

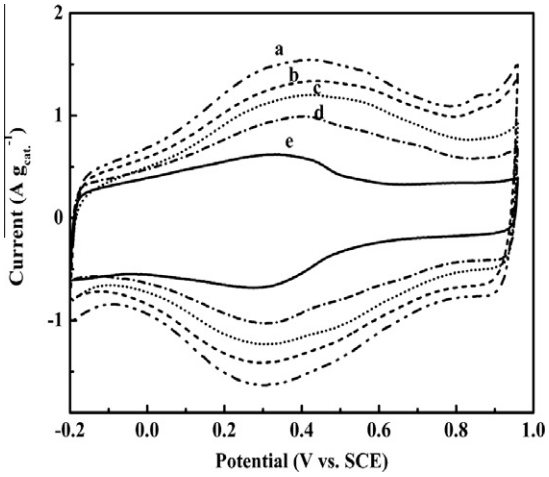

Fig. 7. Cyclic voltammograms of RuO_xH_y/MWCNTs (Ru loading: 3.9 wt.%) in 0.5 M H_2SO_4 after pretreatments in the narrow potential range (−0.20 to 0.46 V) in 0.5 M H_2SO_4 (a) without or (b) with the presence of 0.5 M CH_3OH, and in the extended potential range (−0.20 to 0.96 V) in 0.5 M H_2SO_4 (c) without or (d) with the presence of 0.5 M CH_3OH. (e) Shows the reference cyclic voltammogram for a "pure" MWCNT support.

MWCNTs-based electrode (Fig. 7e), that the broad capacitive feature characteristic of RuO_xH_y in the RuO_xH_y/MWCNT electrode always remained evident after the different pretreatments. This is strong evidence supporting that the nature of RuO_xH_y species in the RuO_xH_y/MWCNT electrode did not change during the pretreatments.

3.2.2. Pt–$(RuO_xH_y)_m$/MWCNTs

Fig. 8 shows the CV curves of Pt–$(RuO_xH_y)_m$/MWCNT electrodes in 0.5 M H_2SO_4. The voltammetric features in the potential range between –0.20 and 0.10 V, usually referred to as "hydrogen adsorption/desorption" peaks, were widely different for the investigated catalysts. Three hydrogen adsorption/desorption peaks characteristic of polycrystalline Pt surfaces [38] were clearly observed on the reference Pt/MWCNT electrode (i.e., $m = 0$). These peaks became less resolved, and the electrochemically active surface area of Pt (EAS, derived from the hydrogen desorption peaks) decreased with the increase in m (or RuO_xH_y loading) in Pt–$(RuO_xH_y)_m$/MWCNT electrodes (Fig. 8, Table 3), indicative of a decrease in the fraction of exposed Pt atoms. For Pt–$(RuO_xH_y)_m$/MWCNT electrodes subjected to the pretreatment in the extended potential range, the hydrogen adsorption/desorption features changed to approach those on the reference Pt/MWCNTs (Fig. 8B). Their derived EAS data were consistently larger than those of their counterpart electrodes pretreated in the narrow potential range (Fig. 8A), especially at $m \geqslant 0.20$. These observations indicate an increased recovery of active Pt surface and are compatible with the RuO_xH_y dissolution during the pretreatment in the extended potential range.

In separate experiments, the electrolyte solutions after the pretreatment in extended potential range were sampled and analyzed by ICP-MS to quantitatively check the dissolution of RuO_xH_y from the two Pt–$(RuO_xH_y)_m$/MWCNT electrodes of $m =$ 0.10 and 0.20. The amount of ruthenium detected in the electrolyte corresponded to ca. 70% and 55%, respectively.

A referee of this present paper was wondering if the loss of ruthenium occurred evenly throughout a pretreatment or mainly at the beginning and if ruthenium loss would continue to occur during methanol oxidation. He/she kindly advised us to provide information about kinetics of the ruthenium dissolution at varying potentials applied. The Pt–$(RuO_xH_y)_{0.20}$/MWCNT electrode was cycled accordingly in 0.5 M H_2SO_4 solution for up to 100 cycles with potential up-limits at $E_a = 0.46$, 0.66 and 0.96 V, respectively. Fig. 9 shows the kinetics of RuO_xH_y dissolution by correlating the relative content of ruthenium with the number of potential sweep cycles. It is apparent that the rate of ruthenium dissolution depends greatly on the potential up-limit and the number of cycles. No ruthenium dissolution was detected when the potential up-limit was set no higher than $E_a = 0.46$ V. The dissolution became increasingly significant when the electrode was cycled to higher potentials; the total loss of ruthenium was more than 30% and 50%, respectively, when the potential up-limit was increased to

Table 2
Effect of pretreatment potentials on the capacitive property of RuO_xH_y/MWCNTs (Ru loading: 3.9 wt.%).

Pretreatment potential range	Pretreatment electrolyte	C(RuO_xH_y/MWCNTs)[a] (F g_{cat}^{-1})	C(RuO_xH_y)[b] (%)	C_L(RuO_xH_y)[c] (%)
0.20–0.46 V	0.5 M H_2SO_4	136	100	0
	0.5 M H_2SO_4 + 0.5 M CH_3OH	119	82	18
0.20–0.96 V	0.5 M H_2SO_4	104	66	34
	0.5 M H_2SO_4 + 0.5 M CH_3OH	83	44	56

[a] Mass-specific capacitance of RuO_xH_y/MWCNT sample. The mass-specific capacitance of MWCNTs obtained in Fig. 7e is 45 F g^{-1}.
[b] Percentage of RuO_xH_y evaluated by the capacitance.
[c] Percentage of RuO_xH_y loss after pretreatment specified; the loss of capacitance due to CH_3OH/H_2O exchange was included also in the RuO_xH_y loss.

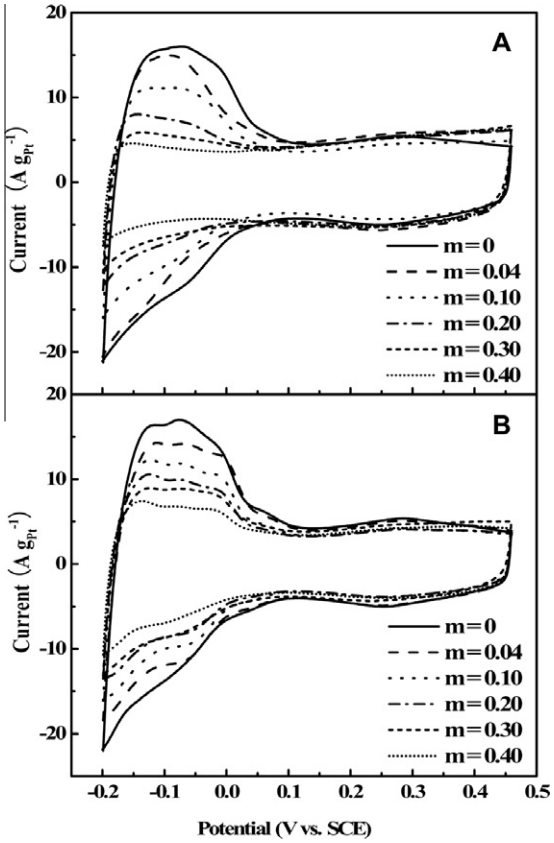

Fig. 8. Cyclic voltammograms of Pt–$(RuO_xH_y)_m$/MWCNTs in 0.5 M H_2SO_4 after the pretreatments in (A) narrow (−0.20 to 0.46 V) and (B) extended (−0.20 to 0.96 V) potential ranges.

Table 3
Electrochemically active surface area, and activity for CO and methanol electro-oxidation of Pt in Pt–$(RuO_xH_y)_m$/MWCNT catalysts after the pretreatment in the narrow and extended potential ranges.

m[a]	Pretreatment (−0.20 to 0.46 V)					Pretreatment (−0.20 to 0.96 V)					
	EAS[b] ($m^2\ g_{Pt}^{-1}$)	E_o[c] (V)	E_p[d] (V)	MSA[e] ($A\ g_{Pt}^{-1}$)	IA[g] ($A\ m^{-2}$)	EAS[b] ($m^2\ g_{Pt}^{-1}$)	E_o[c] (V)	E_p[d] (V)	I_f/I_b[f]	MSA[e] ($A\ g_{Pt}^{-1}$)	IA[g] ($A\ m^{-2}$)
0	66.0	0.36	0.60	3.5	0.05	69.0	0.44	0.60	0.59	13.2	0.19
0.04	56.4	0.30	0.52	20.4	0.36	59.6	0.35	0.60	0.63	5.9	0.10
0.10	43.6	0.25	0.48	30.9	0.71	49.2	0.28	0.59	0.69	15.8	0.32
0.20	29.3	0.24	0.43	17.0	0.58	41.0	0.26	0.58	0.69	18.3	0.45
0.30	22.1	0.27	0.47	8.8	0.40	36.3	0.22	0.54	0.68	13.6	0.37
0.40	14.7	0.33	0.51	2.9	0.20	26.2	0.25	0.56	0.71	7.7	0.29

[a] Atomic Ru/Pt ratio of as-prepared Pt–$(RuO_xH_y)_m$/MWCNTs.
[b] Electrochemically active surface area.
[c] Onset potential (E_o) for CO stripping in 0.5 M H_2SO_4 electrolyte.
[d] Peak potential (E_p) for CO stripping in 0.5 M H_2SO_4 electrolyte.
[e] Mass-specific activity obtained from the chronoamperometry measurement at 0.4 V (vs. SCE) at the time of 60 min (see Fig. 11).
[f] Ratio of the anodic peak currents in the forward (I_f) and the reverse (I_b) scans of methanol electro-oxidation.
[g] Intrinsic activity obtained from the chronoamperometry measurement at 0.4 V (vs. SCE) at the time of 60 min (see Fig. 11).

E_a = 0.66 and 0.96 V. With either of these two potential up-limits, the dissolution of RuO_xH_y was very fast during the first 30 cycles and then slowed down gradually on further increasing the sweep cycles up to the 60th cycle. No further ruthenium dissolution was detected later, which indicates that the electrode catalyst was basically stabilized for the electrochemical study, as evidenced by the invariant CV curves after the 60th cycle (data not shown here). That is the basis why our pretreatments to the electrodes were "standardized" by conducting 60 cycles in the narrow (−0.20 to 0.46 V, or E_a = 0.46 V) and extended (−0.20 to 0.96 V, or E_a = 0.96 V) potential ranges.

Fig. 10 shows the CO stripping voltammograms on Pt–$(RuO_xH_y)_m$/MWCNT catalysts, their onset (E_o) and peak potentials (E_p) for the CO electro-oxidation are given in Table 3. Though the numbers of E_o and E_p were affected by the value of m, they were consistently lower on the catalysts containing RuO_xH_y than on the reference ruthenium-free catalyst (m = 0). When the pretreatment was conducted in the narrow potential range (Fig. 10A), even a very small amount of RuO_xH_y (e.g., m = 0.04) could effect substantial lowering of E_o and E_p for the electro-oxidation of adsorbed CO. As is seen in Fig. 10A, both E_o and E_p shifted continuously toward lower potentials on increasing the amount of RuO_xH_y up to m = 0.20. Specifically, the numbers of E_o (0.24 V) and E_p (0.43 V) for CO oxidation on Pt–$(RuO_xH_y)_{0.20}$/MWCNTs were lowered by 0.12 and 0.17 V, respectively, relative to those on the reference Pt/MWCNT electrode (see also Table 3). However, the E_o and E_p were shifted back toward some higher potentials on further increase in the amount of RuO_xH_y up to m = 0.40, when compared with the case of m = 0.20.

The CO stripping voltammograms shown in Fig. 10B were obtained on the samples after the pretreatment in the extended potential range. Compared with their counterparts pretreated in the narrow potential range (see Fig. 10A), the promotional effect of RuO_xH_y seemed to be significantly "weakened". The E_o and E_p of the CO stripping peaks were apparently positive-shifted (Table 3), becoming more close to those on the reference Pt/MWCNT electrode when the amount of RuO_xH_y before the pretreatment was low (i.e., m < 0.20). These phenomena were in consistent with the

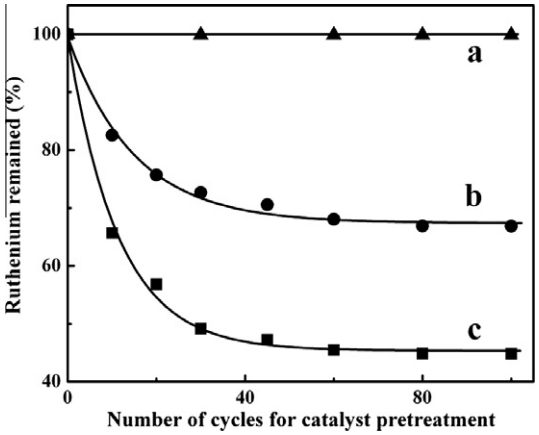

Fig. 9. Dissolution of ruthenium from Pt–$(RuO_xH_y)_{0.20}$/MWCNT electrode during the pretreatments by potential sweep cycling with varying potential up-limits (E_a) in 0.5 M H_2SO_4. E_a = 0.46 (a), 0.66 (b) and 0.96 V (c).

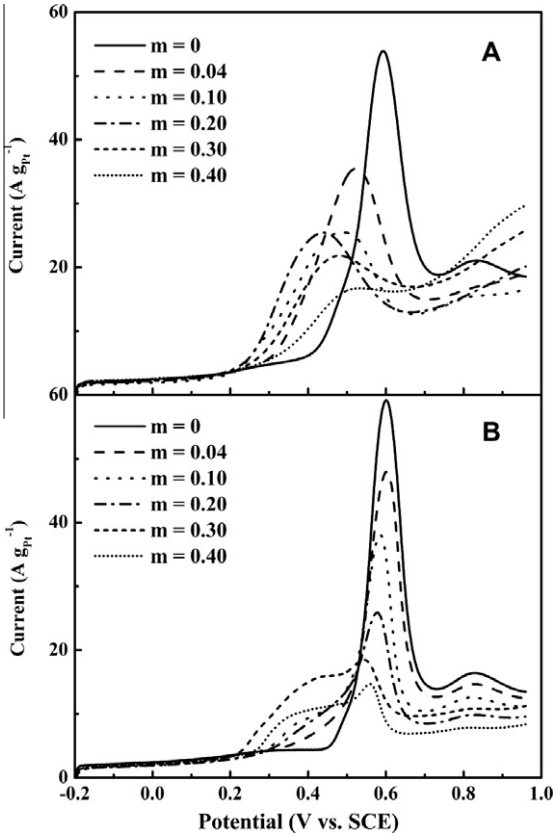

Fig. 10. CO stripping voltammograms of Pt–$(RuO_xH_y)_m$/MWCNTs in 0.5 M H_2SO_4 after the pretreatments in (A) narrow (−0.20 to 0.46 V) and (B) extended (−0.20 to 0.96 V) potential ranges.

results presented in the preceding paragraphs of this section that significant RuO_xH_y dissolution had happened during the pretreatment in the extended potential range.

3.2.3. Pt–$(RuO_xH_y)_m$/MWCNTs for methanol electro-oxidation

Fig. 11 shows the CV curves of methanol electro-oxidation on the Pt–$(RuO_xH_y)_m$/MWCNT electrodes in the narrow and extended potential ranges after the standardized pretreatments. Since the CV curves obtained in the narrow potential range did not allow the detection of methanol oxidation peaks either in the forward or in the reverse scans, the current was plotted in Fig. 10A as a function of potential in the positive scans for the sake of clarity. According to the methanol electro-oxidation current, the activity of Pt in the Pt–$(RuO_xH_y)_m$/MWCNT catalysts changed remarkably with the amount of RuO_xH_y, and the maximum activity was obtained at $m = 0.10$. The activity decrease at higher m values could be ascribed to the loss of active Pt surface (EAS, Table 3) for the electrochemical reaction.

The methanol electro-oxidation CV curves obtained on Pt–$(RuO_xH_y)_m$/MWCNT catalysts after the pretreatment in the extended potential range manifested clear anodic peaks in both forward and reverse scans (Fig. 11B). The ratio of peak currents on the forward (I_f) and reverse (I_b) scans could be regarded as an indicator of the "cleanness" of the catalyst surface from poisonous carbon-containing species [39]. This ratio (I_f/I_b) was given in Table 3 and was used to evaluate the anti-poison property of the Pt–$(RuO_xH_y)_m$/MWCNT catalysts shown in Fig. 10B. The lowest I_f/I_b ratio (0.59) over the reference Pt/MWCNTs was indeed in line with a poor anti-poison property of the unpromoted Pt in this catalyst. However, this I_f/I_b ratio was enhanced significantly by the presence of even a very small amount of RuO_xH_y. For instance, the ratio on Pt–$(RuO_xH_y)_{0.04}$/MWCNTs was 0.63, not to mention that residual RuO_xH_y in the working electrode could be significantly lower because of RuO_xH_y dissolution during the pretreatment. The ratio became as high as $I_f/I_b = 0.70$ on every other Pt–$(RuO_xH_y)_m$/MWCNT catalyst ($m = 0.10$–0.40), indicating a further improved anti-poison property of these RuO_xH_y-promoted Pt catalysts.

The electrocatalytic activities of Pt in these pretreated Pt–$(RuO_xH_y)_m$/MWCNT catalysts (Fig. 11B) were all lower than that in the reference Pt/MWCNT catalyst, except for Pt–$(RuO_xH_y)_{0.20}$/MWCNTs. Also, the activity sequence of these Pt–$(RuO_xH_y)_m$/MWCNT catalysts was very different from that of their counterparts in Fig. 11A. RuO_xH_y dissolution during the pretreatment in the extended potential range could be the main cause for this difference. In fact, our ICP-MS measurement of ruthenium content in the electrolyte solution of the most active Pt–$(RuO_xH_y)_{0.20}$/MWCNT catalyst in Fig. 10B disclosed that a half (55%) of RuO_xH_y in the catalyst had dissolved into the electrolyte solution during the pretreatment in the extended potential range. Therefore, the actual RuO_xH_y content in this most active Pt–$(RuO_xH_y)_{0.20}$/MWCNTs (Fig. 10B) was $m = 0.09$. Interestingly, this number agreed well with that of the most active Pt–$(RuO_xH_y)_{0.10}$/MWCNT catalyst in Fig. 11A, where the catalyst pretreatment was conducted in the narrow potential range.

Fig. 12 shows the CA performance for methanol oxidation of the Pt–$(RuO_xH_y)_m$/MWCNT catalysts under a constant potential of 0.40 V. All of the catalysts featured a pronounced current decay in the first 10–20 min, which could arise from the accumulation of poisonous intermediates such as species containing –CO, –CHO and/or $–CH_2OH$ functionality [40]. The current decay slowed down

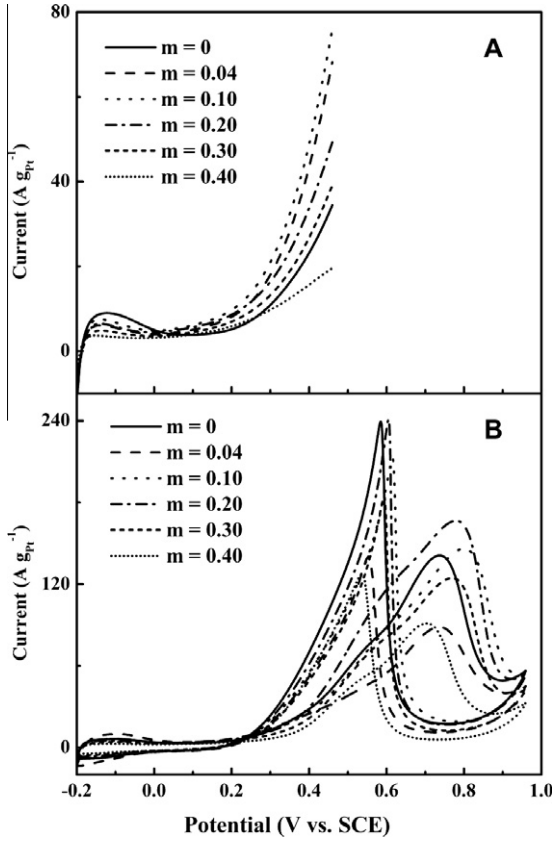

Fig. 11. Cyclic voltammograms of Pt–$(RuO_xH_y)_m$/MWCNTs in 0.5 M H_2SO_4 + 0.5 M CH_3OH after the pretreatments in (A) narrow (−0.20 to 0.46 V) and (B) extended (−0.20 to 0.96 V) potential ranges. Only the forward scan curve is shown in (A).

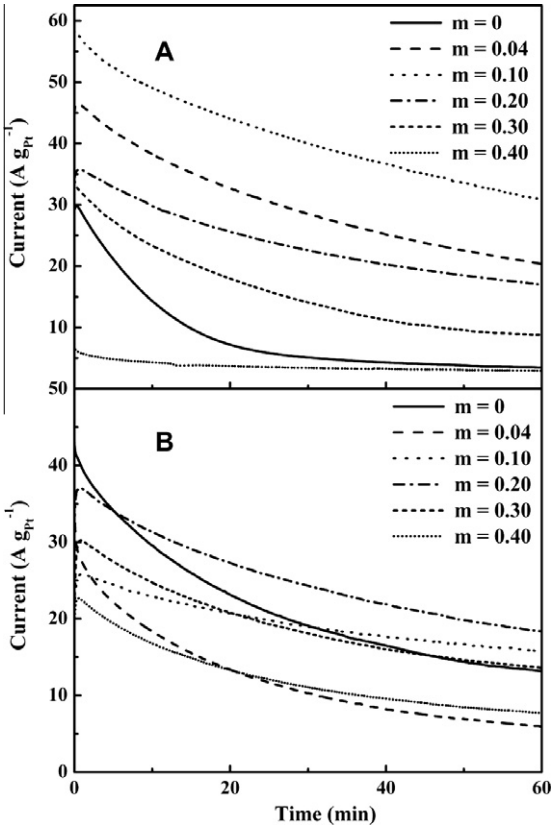

Fig. 12. Chronoamperograms of Pt–$(RuO_xH_y)_m$/MWCNTs in 0.5 M H_2SO_4 + 0.5 M CH_3OH at 0.40 V after the pretreatments in (A) narrow (−0.20 to 0.46 V) and (B) extended (−0.20 to 0.96 V) potential ranges.

but was still observable at longer times, which might be associated with the adsorption of SO_4^{2-} anions on the catalyst surface and/or mass transport effects [26,41]. The initial current decay was much more pronounced on the reference Pt/MWCNT electrode ($m = 0$), which lost nearly 50% current in the first 20 min.

When the pretreatment was carried out in the narrow potential range, the activity sequence of Pt–$(RuO_xH_y)_m$/MWCNTs in the CA tests (Fig. 12A) always agreed with the order in the CV measurements (Fig. 11A). When these Pt–$(RuO_xH_y)_m$/MWCNT catalysts were subjected to the pretreatment in the extended potential range, however, the activity order based on CA tests (Fig. 12B) was not consistent with that based on the CV measurements (Fig. 11B). Despite this disagreement, Pt–$(RuO_xH_y)_{0.20}$/MWCNTs exhibited consistently the highest activity in both measurements.

The mass-specific activity (MSA) and intrinsic activity (IA) data of Pt in Pt–$(RuO_xH_y)_m$/MWCNTs are also listed in Table 3. These activity data were obtained as the currents recorded at the time of 60 min in Fig. 12. Quantitatively, the MSA and IA data of the most active catalyst after the pretreatment in the narrow potential range (i.e., Pt–$(RuO_xH_y)_{0.10}$/MWCNTs) were enhanced by an order of magnitude (9 times increase in MSA and 14 times in IA) compared with the reference Pt/MWCNT catalyst ($m = 0$), due to the promotional effect of RuO_xH_y. By contrast, the MSA and IA data of the most active catalyst after the pretreatment in the extended potential range (i.e., Pt–$(RuO_xH_y)_{0.20}$/MWCNTs) were, respectively, 1.4 and 2.2 times those of the reference Pt/MWCNT catalyst. Interestingly, the activity orders in terms of MSA and IA were consistent with each other with the only exception at Pt–$(RuO_xH_y)_{0.40}$/MWCNTs pretreated in the narrow potential range, the MSA of Pt in this sample was even lower than the reference Pt/MWCNT catalyst due to severe encapsulation of Pt by RuO_xH_y.

4. Discussion

The present data from comprehensive characterizations by XRD, XPS, H_2-TPR and TGA (Figs. 1–4) are consistent in showing that the as-prepared Pt–$(RuO_xH_y)_m$/MWCNT samples in this study contained no metallic Ru and RuO_2 crystallite but only amorphous hydrous ruthenium oxide, which can be expressed as either $RuO_2{\cdot}nH_2O$ or RuO_xH_y. Ruthenium in this RuO_xH_y species is characterized as a mixed valence state between +3 and +4 and can behave as a mixed electron/proton conductor innately related with the Ru–OH speciation [42,43]:

$$Ru^{IV}{-}O^{2-} + H^+ + e^- \rightleftharpoons Ru^{III}{-}OH$$

CO stripping voltammetry is considered as an in situ approach to study the promoter function in Pt-based electrocatalysts in electrochemical environments [17,21,26] and has often been used to evaluate the anti-poison or CO tolerance property of electrocatalysts. The present CV measurements of the Pt-free RuO_xH_y/MWCNT samples (Figs. 6 and 7) clearly demonstrate that RuO_xH_y itself is inert for hydrogen and CO chemisorptions and is completely inactive for methanol electro-oxidation at potentials lower than 0.85 V. However, its co-presence with Pt in the Pt–$(RuO_xH_y)_m$/MWCNT samples induced significant lowering of the E_o and E_p on the CO stripping curves (Fig. 10, Table 3), compared to the case without its presence (i.e., on the reference Pt/MWCNTs). Thus, the following modified bifunctional mechanism can be proposed to explain the observed RuO_xH_y promotion of Pt for CO removal:

$$Pt{-}CO_{ads} + Ru^{III}{-}OH + H_2O \rightarrow Pt + Ru^{IV}{-}O^{2-} + 3H^+ + 3e^- + CO_2$$

The peculiarity of RuO_xH_y as a mixed electron/proton conductor would easily delocalize the protons and electrons. On the other hand, the required water molecule for this reaction does not necessarily have to come directly from the electrolyte solution; it can also come from the structure of RuO_xH_y:

$$Pt{-}CO_{ads} + RuO_xH_y \rightarrow Pt + RuO_{x-1}H_{y-2} + CO_2 + 2H^+ + 2e^-$$

Pt–$(RuO_xH_y)_{0.20}$/MWCNTs was identified as the most efficient catalyst for this catalysis since it produced the lowest E_o and E_p on the CO stripping voltammogram. As the domain size of RuO_xH_y entities increased with m in Pt–$(RuO_xH_y)_m$/MWCNT samples (Fig. 5), the weakening of RuO_xH_y promotion of Pt for the CO removal at $m > 0.20$ could be probably due to a self-aggregation of the promoter to form bigger RuO_xH_y particles that changed the proximity between RuO_xH_y and Pt.

Anodic CV scanning up to a reasonably high potential (such as 0.96 V) has been frequently used to clean and activate the anode catalysts for electrochemical reactions [44]. It was alerted earlier, however, that dissolution of ruthenium species in anode PtRu/C catalyst might take place at potentials higher than 0.46 V [45,46]. This possibility of ruthenium dissolution is demonstrated clearly in this work by comparing the electrochemical performance of RuO_xH_y/MWCNTs (Fig. 7) and Pt–$(RuO_xH_y)_m$/MWCNTs (Fig. 8) after they were subjected to the "standard" pretreatments both in the narrow (−0.20 to 0.46 V) and in the extended (−0.20 to 0.96 V) potential ranges. It is now clear that the pretreatment in the narrow potential range induced no ruthenium dissolution, but the pretreatment in the extended potential range caused significant dissolution of RuO_xH_y from the electrodes. Quantitatively, the electrodes of Pt–$(RuO_xH_y)_m$/MWCNTs with $m = 0.10$ and 0.20 were confirmed, respectively, to lose 70% and 55% of their RuO_xH_y during the pretreatment in the extended potential range.

The electro-oxidation of methanol over the present Pt–$(RuO_xH_y)_m$/MWCNT catalysts would involve the following key steps:

$$CH_3OH + Pt \rightarrow Pt{-}CO_{ads} + 4H^+ + 4e^-$$

$$Pt{-}CO_{ads} + RuO_xH_y \rightarrow Pt + RuO_{x-1}H_{y-2} + CO_2 + 2H^+ + 2e^-$$

Since the average sizes of Pt crystallites (ca. 2.7 nm) from the XRD measurements did not change significantly in the as-prepared Pt–$(RuO_xH_y)_m$/MWCNT samples, the following discussion on RuO_xH_y promotion of Pt in these samples is made by assuming no change in the sizes of Pt.

In the absence of RuO_xH_y dissolution (i.e., when the pretreatment of the electrode catalyst was conducted in the narrow potential range), the MSA and IA data of Pt in Pt–$(RuO_xH_y)_m$/MWCNTs for methanol electro-oxidation were seen to increase remarkably with m up to $m = 0.10$ and then to decrease at higher m (Fig. 11A and 12A, Table 3). As is discussed on RuO_xH_y promotion of Pt for the CO stripping catalysis, these data would indicate that an appropriate m number or a suitable Pt–RuO_xH_y proximity is also required for maximizing the activity of Pt for the methanol electro-oxidation. The activity of Pt in the most active Pt–$(RuO_xH_y)_{0.10}$/MWCNTs was enhanced by a factor of 9 in MSA and 14 in IA, respectively, when compared with the reference Pt/MWCNT catalyst. It should be mentioned that the most efficient Pt–$(RuO_xH_y)_{0.20}$/MWCNT catalyst in the CO stripping measurements (Fig. 10A, Table 3) failed to show the highest activity for methanol electro-oxidation. This fact suggests that the suitable Pt–RuO_xH_y proximity required for the CO removal catalysis in Pt–$(RuO_xH_y)_m$/MWCNTs was somewhat different from that required for the methanol electro-oxidation catalysis. Significantly negative effect was noted when a large excess of RuO_xH_y was present in the Pt–RuO_xH_y/MWCNT catalyst. For instance, Pt–$(RuO_xH_y)_{0.40}$/MWCNTs became even inferior to the reference Pt/MWCNT catalyst in terms of MSA, which could be at least partly due to an increased blocking by RuO_xH_y of the active Pt surface at high Ru loadings. Consequently, the presence of RuO_xH_y would produce two opposite effects on the electrocatalysis of Pt, as shown by the data summarized in Table 3. The positive effect is

reflected by its promotion on CO removal from the Pt surface and its enhancement of Pt activity for methanol electro-oxidation, and the negative one is characterized by a continuous decrease in EAS of Pt with increasing *m*. However, an optimization in the proximity between Pt particles and RuO_xH_y entities seems insufficient for the positive effect of RuO_xH_y, since the IA data of Pt (Table 3) did not remain constant after the optimization at $m = 0.10$ but decreased continuously with further increase in *m*. Electronic and perhaps other effects could also be involved in inducing the change of IA at $m > 0.10$, which remained unclear at the present stage.

The situation became quite complex when the catalyst pretreatment was done in the extended potential range, which caused significant dissolution of RuO_xH_y into the electrolyte solution. In this case (see the right half of Table 3), Pt–$(RuO_xH_y)_{0.20}$/MWCNTs showed the highest activity for methanol electro-oxidation, whereas Pt–$(RuO_xH_y)_{0.30}$/MWCNTs became the most efficient catalyst for the CO removal. Although after the pretreatment in the extended potential range the composition and EAS of the most active Pt–$(RuO_xH_y)_{0.20}$/MWCNTs (in the right half of Table 3) became, due to RuO_xH_y dissolution, very close to those of the most active Pt–$(RuO_xH_y)_{0.10}$/MWCNTs after the pretreatment in the narrow potential range (in the left half of Table 3), the MSA and IA data of the former catalyst were both significantly lower for the electro-oxidation of methanol. In fact, most of the Pt–$(RuO_xH_y)_m$/MWCNT samples pretreated in the extended potential range showed lower IA than their counterparts pretreated in the narrow potential range. This observation cannot be explained only by the dissolution of RuO_xH_y since the number of IA for the RuO_xH_y-free Pt/MWCNT catalyst after the pretreatment in the extended potential range was even enhanced by a factor of 4 compared with its counterpart pretreated in the narrow potential range.

Therefore, it seems quite reasonable that the pretreatment conducted in the extended potential range induced not only ruthenium dissolution but also significant change in the surface property of Pt. The development of "hydrogen adsorption/desorption" features on Pt–$(RuO_xH_y)_m$/MWCNT catalysts to approach those on RuO_xH_y-free Pt/MWCNTs after such pretreatment (Fig. 8B) can be further evidence for the change in the surface structure/property of Pt. The residual RuO_xH_y after such pretreatment would also have a positive effect on the formation of a better Pt surface structure for the electro-oxidation of methanol, which was supported by comparison of the MSA and IA data in the right half of Table 3. For instance, after the pretreatment in the extended potential range, the MSA and IA of the most active Pt–$(RuO_xH_y)_{0.20}$/MWCNTs were still 1.4 and 2.2 times those of the reference catalyst Pt/MWCNTs, respectively.

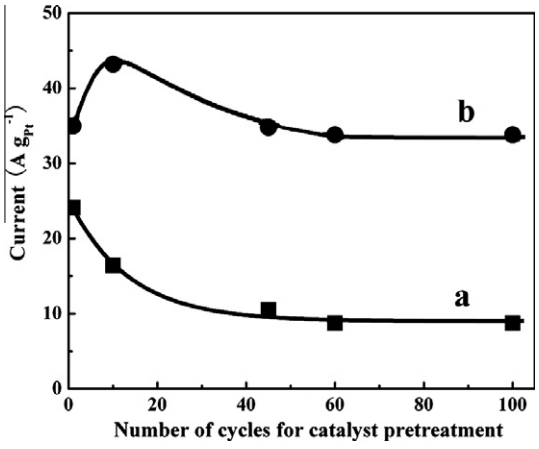

Fig. 13. Correlation of Pt activity in the pretreated Pt–$(RuO_xH_y)_{0.20}$/MWCNT electrode for (a) CO and (b) methanol electro-oxidation with the number of potential sweep cycles for the pretreatment with potential up-limit at $E_a = 0.96$.

The electrode catalyst (Pt–$(RuO_xH_y)_{0.20}$/MWCNTs) subjected to the pretreatments of varied numbers of cycles with the potential up-limit at $E_a = 0.96$ V (Fig. 9c) was also used to study the CO stripping and methanol oxidation catalysis by CV measurements in the extended potential range (−0.20 to 0.96 V) (Supplementary data Figs. S1 and S2). Fig. 13 correlates the Pt activity at 0.40 V for both CO stripping and methanol oxidation catalysis with the number of such pretreatment cycles. With reference to the data shown in Fig. 9, it is clear that the electrocatalytic activity of Pt for both reactions well related with the remained percentage of RuO_xH_y after more than 10 pretreatment cycles, which is in support of the function of RuO_xH_y as the efficient promoter of Pt for the electro-oxidation catalysis. However, it is of interest to note in Fig. 13 that during the first 10 cycles of the pretreatment at $E_a = 0.96$ V, the Pt activity for methanol oxidation even increased to some extent but the activity for CO oxidation decreased significantly, compared with the case of no RuO_xH_y dissolution (i.e., data at the zero-cycle). These facts suggest again that the Pt–RuO_xH_y proximity required for the two reactions was different, and the pretreatment up to a potential as high as 0.96 V could modify the property of Pt, in addition to the RuO_xH_y dissolution.

It has been known that the surface of a Pt anode catalyst would undergo an irreversible oxidation process when the anodic potential limit of CV measurement was extended to higher than 0.71 V vs. SCE (0.95 V vs. NHE) [47]. In an earlier work by Hu and Liu [48], the application of repeated CV scanning to Pt electrodes in −0.24 to 1.26 V was shown effective in inducing changes in the redox reversibility of Pt surfaces, which resulted in significant activity improvement of Pt for methanol electro-oxidation. In this work, the activity improvement in Pt/MWCNTs after the pretreatment in the extended potential range for methanol electro-oxidation, as shown in the right half of Table 3, seems to be in line with those observations. Thus, it seems conclusive that the structure/property change to Pt induced by the pretreatment of Pt–$(RuO_xH_y)_m$/MWCNTs in the extended potential range can be indeed an important aspect. In addition to RuO_xH_y dissolution, for understanding the change of the activity data in Table 3. However, more powerful surface-specific and in situ measurements would be required to gain further insights into the details of such surface structure change.

We checked also in separate experiments if, after the "standard" pretreatment of the Pt–$(RuO_xH_y)_{0.20}$/MWCNT electrode in the extended potential range, ruthenium dissolution would continue to occur during repeated CV measurements of the methanol electro-oxidation reaction. The results showed that the loss of ruthenium was as low as 5% when the CV measurement was repeated for 110 cycles in the full potential range (−0.20 to 0.96 V), suggesting that the remaining RuO_xH_y promoter in the electrode was reasonably stabilized for methanol electro-oxidation.

5. Conclusions

Our data demonstrate clearly that the RuO_xH_y (hydrous ruthenium oxide) alone, without co-presence of other ruthenium entities (metallic Ru or anhydrous RuO_2), can act as an efficient promoter of Pt in Pt–RuO_xH_y/MWCNT materials for the electro-oxidation of CO and methanol. The promotion of RuO_xH_y in the electrocatalysis depended on the proximity and relative amount of RuO_xH_y and Pt and was affected significantly by the pretreatment potentials. Severe dissolution of the RuO_xH_y promoter from the catalysts was identified when the electrode was pretreated by repeated CV scanning in the extended potential range (−0.20 to 0.96 V) but was not detected when the potential up-limit of the

pretreatment was set no higher than 0.46 V. The RuO_xH_y dissolution would change not only the proximity and relative amount of RuO_xH_y and Pt but also the surface structure of Pt. Further work is needed to uncover factors governing the mobility and stability of RuO_xH_y and Pt during the pretreatments.

Acknowledgments

This work is supported by NSF(20773074, 20921001) and MOST (2006AA03Z225) of China.

Appendix A. Supplementary material

Supplementary data associated with this article can be found, in the online version, at doi:10.1016/j.jcat.2010.07.021.

References

[1] H.A. Gasteiger, N. Markovic, P.N. Ross Jr., E.J. Cairns, J. Electrochem. Soc. 141 (1994) 1795.
[2] T. Kawaguchi, W. Sugimoto, Y. Murakami, Y. Takasu, J. Catal. 229 (2005) 176.
[3] M.P. Hogarth, G.A. Hards, Platinum Met. Rev. 40 (1996) 150.
[4] M. Watanabe, S. Motoo, J. Electroanal. Chem. Interfacial Electrochem. 60 (1975) 267.
[5] T. Frelink, W. Visscher, A.P. Cox, J.A.R. van Veen, Electrochim. Acta 40 (1995) 1537.
[6] K.L. Ley, R. Liu, C. Pu, Q. Fan, N. Leyarovska, C. Segre, E.S. Smotkin, J. Electrochem. Soc. 144 (1997) 1543.
[7] D. Chu, S. Gilman, J. Electrochem. Soc. 143 (1996) 1685.
[8] A. Hamnett, Catal. Today 38 (1997) 445.
[9] A. Hamnett, B. Kennedy, Electrochim. Acta 33 (1988) 1613.
[10] A.S. Arico, P. Creti, H. Kim, R. Mantegna, N. Giordano, V. Antonucci, J. Electrochem. Soc. 143 (1996) 3950.
[11] A.H.C. Sirk, J.M. Hill, S.K.Y. Kung, V.I. Birss, J. Phys. Chem. B 108 (2004) 689.
[12] D.R. Rolison, P.L. Hagans, K.E. Swider, J.W. Long, Langmuir 15 (1999) 774.
[13] J.W. Long, R.M. Stroud, K.E. Swider-Lyons, D.R. Rolison, J. Phys. Chem. B 104 (2000) 9772.
[14] H.M. Villullas, F.I. Mattos-Costa, L.O.S. Bulhoes, J. Phys. Chem. B 108 (2004) 12898.
[15] L. Cao, F. Scheiba, C. Roth, F. Schweiger, C. Cremers, U. Stimming, H. Fuess, L. Chen, W.T. Zhu, X.P. Qiu, Angew. Chem. Int. Ed. 45 (2006) 5315.
[16] S. Huang, C. Chang, K. Wang, C. Yeh, ChemPhysChem 8 (2007) 1774.
[17] J. Zeng, J.Y. Lee, Mater. Chem. Phys. 104 (2007) 336.
[18] K.I.B. Eguiluz, G.R. Salazar-Banda, D. Miwa, S.A.S. Machado, L.A. Avaca, J. Power Sources 179 (2008) 42.
[19] J.L. Gomez de la Fuente, M.V. Martinez-Huerta, S. Rojas, P. Hernandez-Fernandez, P. Terreros, J.L.G. Fierro, M.A. Pena, Appl. Catal. B: Environ. 88 (2009) 505.
[20] Q. Lu, B. Yang, L. Zhuang, J. Lu, J. Phys. Chem. B 109 (2005) 1715.
[21] H.N. Dinh, X. Ren, F.H. Garzon, P. Zelenay, S. Gottesfeld, J. Electroanal. Chem. 491 (2000) 222.
[22] H. Kim, I. Rabelo de Moraes, G. Tremiliosi-Filho, R. Haasch, A. Wieckowski, Surf. Sci. 474 (2001) L203.
[23] C. Bock, A. Collier, B. MacDougall, J. Electrochem. Soc. 152 (2005) A2291.
[24] P. Chen, H.B. Zhang, G.D. Lin, Q. Hong, K.R. Tasi, Carbon 35 (1999) 1495.
[25] X.M. Wu, Y. Wang, K.M. Dong, J.M. Zhou, G.D. Lin, H.B. Zhang, Acta Chim. Sin. 63 (2005) 484.
[26] L. Li, G. Wu, B.Q. Xu, Carbon 44 (2006) 2973.
[27] X. Fu, H. Yu, F. Peng, H. Wang, Y. Qian, Appl. Catal. A: Gen. 321 (2007) 190.
[28] L. Li, H.X. Wang, B.Q. Xu, J.L. Li, W. Xing, Z.Q. Mao, Acta Phys. Chim. Sin. 19 (2003) 342.
[29] J.P. Zheng, P.J. Cygan, T.R. Jow, J. Electrochem. Soc. 142 (1995) 2699.
[30] B. Yang, Q.Y. Lu, Y. Wang, L. Zhuang, J.T. Lu, P.F. Liu, J.B. Wang, R.H. Wang, Chem. Mater. 15 (2003) 3552.
[31] S. Kundu, Y. Wang, W. Xia, M. Muhler, J. Phys. Chem. C 112 (2008) 16869.
[32] S. Huang, S. Chang, C. Yeh, J. Phys. Chem. B 110 (2006) 234.
[33] S. Sarangapani, B.V. Tilak, C.P. Chen, J. Electrochem. Soc. 143 (1996) 3791.
[34] K.E. Swider, C.I. Merzbacher, P.L. Hagans, D.R. Rolison, J. Non-Cryst. Solids 225 (1998) 348.
[35] V. Radmilović, H.A. Gasteiger, P.N. Ross Jr., J. Catal. 154 (1995) 98.
[36] S. Trasatti, G. Buzzanca, J. Electroanal. Chem. Interfacial Electrochem. 29 (1971) 1.
[37] F. Scheiba, M. Scholz, L. Cao, R. Schafranek, C. Roth, C. Cremers, X.P. Qiu, U. Stimming, H. Fuess, Fuel Cells 6 (2006) 439.
[38] C.H. Hamann, A. Hamnett, W. Vielstich, Electrochemistry, second ed., Wiley-VCH, Weinheim, 1998.
[39] R. Manoharan, J.B. Goodenough, J. Mater. Chem. 2 (1992) 875.
[40] J.W. Guo, T.S. Zhao, J. Prabhuram, R. Chen, C.W. Wong, J. Power Sources 156 (2006) 345.
[41] J. Jiang, A. Kucernak, J. Electroanal. Chem. 543 (2003) 187.
[42] A. Yamada, J.B. Goodenough, J. Electrochem. Soc. 145 (1998) 737.
[43] W. Dmowski, T. Egami, K.E. Swider-Lyons, C.T. Love, D.R. Rolison, J. Phys. Chem. B 106 (2002) 12677.
[44] H.A. Gasteiger, N. Markovic, P.N. Ross Jr., E.J. Cairns, J. Phys. Chem. 98 (1994) 617.
[45] H.A. Gasteiger, N. Markovic, P.N. Ross Jr., E.J. Cairns, J. Phys. Chem. 97 (1993) 12020.
[46] J. McBreen, S. Mukerjee, J. Electrochem. Soc. 142 (1995) 3399.
[47] B.E. Conway, Prog. Surf. Sci. 49 (1995) 331.
[48] C.C. Hu, K.Y. Liu, Electrochim. Acta 44 (1999) 2727.